Composites Communications 36 (2022) 101395

Contents lists available at ScienceDirect

Composites Communications

journal homepage: www.elsevier.com/locate/coco

Design of grayscale digital light processing 3D printing block by machine learning and evolutionary algorithm

Baowen Zhao [a,b,c], Mengjie Zhang [a,b,c], Le Dong [a,b,c], Dong Wang [a,b,c,*]

[a] Robotics Institute, School of Mechanical Engineering, Shanghai Jiao Tong University, Shanghai, 200240, China
[b] State Key Laboratory of Mechanical System and Vibration, Shanghai Jiao Tong University, Shanghai, 200240, China
[c] Meta Robotics Institute, Shanghai Jiao Tong University, Shanghai, 200240, China

A B S T R A C T

Grayscale digital light processing (DLP) 3D printing method, using grayscale light patterns to adjust the microscale material properties, is a revolutionary technology for future advanced manufacturing. However, the design and optimization method of the grayscale distribution remains elusive. In this paper, we propose an optimization method for grayscale DLP printed rectangular blocks based on a machine learning and evolutionary algorithm. We use an automated finite element model-based evaluation to predict the deformation shapes with arbitrary grayscale distribution, considering the nonlinear mechanical performances. A machine learning model based on recurrent neural networks is trained using the database formed by the finite element method model to enable fast and precise prediction of the deformed shapes. Optimal designs of the deformed shapes are efficiently realized via integrating the machine learning model and evolution algorithm method. Grayscale distributions are optimized to form desired deformations and validated by experiments. This work paves the way for designing and optimizing grayscale digital light processing 3D printed structures.

1. Introduction

3D printing has attracted increasing interest recently and has found wide applications as it improves the freedom to design complex geometries [1–7]. Besides the geometric freedom, the ability to assign multiple material properties precisely during 3D printing is also highly needed. Many multimaterial 3D printing methods have been developed to meet this requirement, such as the multi-nozzle voxelated direct ink writing printer [8,9], multimaterial Polyjet 3D printer [10,11], and multimaterial digital light processing (DLP) 3D printer [12]. Among them, DLP 3D printing enables fast speed and provides a high degree of freedom in structural design and material choices. For example, DLP 3D printing is coupled with *in situ* microfluidic systems to prevent material contamination and multimaterial printing [13]. A high-efficiency high-resolution multi-material printing system is developed to fabricate complex lattice structures [14]. However, the multimaterial DLP methods have difficulties realizing fast material exchange, precise material distributions and strong bonding at the multi-material interface.

In contrast, grayscale DLP printing is a simple yet highly efficient way of distributing different material properties [15–22]. The crosslink density can be adjusted by tuning the light intensity patterns to generate various modulus distributions of the printed layer. Each pixel in a 2D slice image can be assigned to a grayscale value so that the minimal size of the material control is the same as the pixel size theoretically. Besides, interfacial bonding is strong because covalently crosslinking is formed. Fast printing speed is ensured, as material shifting and resin removal are unnecessary. Several studies on grayscale DLP printing have been reported [23–29]. For example, Kuang et al. applied grayscale DLP printing to fabricate functionally graded materials, complex lattices and negative Poisson's ratio metamaterial [30]. Wang et al. used the residual stress built in the grayscale 3D printing to fabricate and design shape-shifting helical structures, leaves, origami and flowers [31]. Valizadeh et al. studied the dependency of the material properties on the grayscale value using a hyperelastic constitutive model [32]. However, the design and optimization method of the grayscale distribution remains elusive due to the large design space.

In this work, we develop an optimization method for grayscale DLP printed rectangular blocks based on a machine learning (ML) and evolutionary algorithm (EA). We use an automated finite element model-based evaluation to predict the deformation shapes with arbitrary grayscale distribution, considering the nonlinear mechanical performances using Mooney-Rivlin constitutive model. A recurrent neural networks (RNN) based machine learning model is trained using the database formed by the FEM model to enable fast and precise prediction of the deformed shapes. Optimal designs of the deformed shapes are efficiently enabled via integrating the ML model and EA method.

* Corresponding author. Robotics Institute, School of Mechanical Engineering, Shanghai Jiao Tong University, Shanghai, 200240, China.
E-mail address: wang_dong@sjtu.edu.cn (D. Wang).

https://doi.org/10.1016/j.coco.2022.101395
Received 2 September 2022; Received in revised form 17 October 2022; Accepted 1 November 2022
Available online 4 November 2022

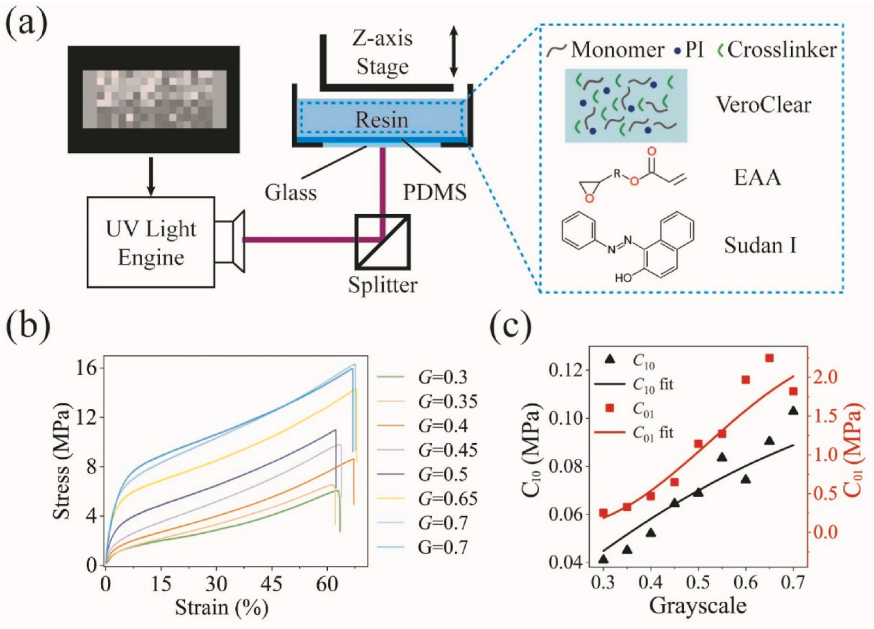

Fig. 1. Grayscale DLP printing. (a) Schematic illustration of the grayscale DLP 3D printing. (b) Uniaxial stress-strain curves of dog-bone-shaped samples printed under various grayscale values ranging from $G = 0.3$ to $G = 0.7$. (c) The dependences of the material parameters C_{10} and C_{01} on the grayscale value.

Grayscale distributions are optimized to form desired deformations and validated by experiments. This work paves the way for the design and optimization of grayscale digital light processing 3D printed structures.

2. Results and discussions

2.1. Grayscale DLP 3D printing

We develop a grayscale DLP printing system composed of a UV-projector (including a 405 nm UV-light source and a DMD module), a 45-degree splitter, a resin tank with a transparent glass window coated with PDMS membrane, and a linearized stepper motor. As shown in Fig. 1(a), the hybrid resin is made by adding epoxy aliphatic acrylate (EAA) to the commercial UV-curable resin VeroClear together with Sudan I as the photo-absorber. Rectangular blocks are printed. A grayscale value G is assigned to each pixel using MATLAB code. $G = 1$ represents full light intensity with RGB (255,255,255), and $G = 0$ means nearly zero light intensity. The grayscale patterns are then transferred to the projector to cure each structure layer.

We then conduct uniaxial tensile tests to obtain the dependence of the material properties on G. A series of "dog-bone" samples are printed with G varying from 0.3 to 0.7. The stress-strain curves of the samples under uniaxial loading are shown in Fig. 1(b). As G increases from 0.3 to 0.7, E increases from 35 MPa to 176 MPa (measured at the strain of 3%). The apparent increase in stiffness results from the higher crosslinking density.

From the stress-strain curves, it can be observed that the materials exhibit nonlinear mechanical behaviors and finite deformation. To capture the material nonlinearity, the Mooney-Rivlin hyperelastic constitutive model is used. The strain energy density function W is

$$W = C_{10}(I_1 - 3) + C_{01}(I_2 - 3) \quad (1)$$

where C_{10} and C_{01} are the material constants, and I_1 and I_2 are the first and the second invariants of the left Cauchy–Green deformation tensor. C_{10} and C_{01} are acquired by fitting the model to experimental data. Fig. 1 (c) demonstrates the correlation between C_{10} and C_{01} and G. Both C_{10} and C_{01} increase with G.

2.2. Machine learning method

We construct an RNN-based ML model to predict the deformed shapes of the rectangular blocks under uniaxial tensile loadings. RNN is a machine learning network suitable for handling sequential data because it uses past information to predict the response of the current and future inputs.

The database in the machine learning algorithm is generated using an automated finite element model-based evaluation. The FEM is run through the commercial finite element software ABAQUS (3DS Dassault Systèmes, France). Clamped boundary conditions are used for the structures. Mooney-Rivlin hyperelastic constitutive model is used. A rectangular block (32×16 mm) is divided into 16×8 elements in the simulation, as shown in Fig. 2(a). Each element is assigned a grayscale value G, which varies from 0.3 to 0.7. The reasons for choosing G between 0.3 and 0.7 are: (1) the modulus change is around one orders of magnitude when G changes from 0.3 to 0.7; (2) the failure strain of the sample printed using G between 0.3 and 0.7 are close, ensuring the fabrication and testing stability. A custom Python code is written to assign different material properties for each element. The size of each database is chosen as 3000. A simple random sampling strategy is used. The calculation time for each sample using FEM is around 15 s, and the total time for evaluating the 3000 designs is around 12 h. Efficient sampling strategies such as sequential sampling could be used for future work. The database is split into the training sets (66.7%) and the test sets (33.3%).

An RNN-based ML model is constructed to train and test databases in Python. The network architecture consists of a sequence input layer, four long short-term memory (LSTM) network layers and a fully connected layer. LSTM is a special type of RNN, which solves the problem of gradient disappearance or explosion in long sequences. The input data for architecture are the grayscale values of each element. The top, central and bottom node deformations are the output data. As shown in Fig. 2(b), a column of grayscale values is treated as a box represented by a single number-array input (size 8). Therefore, the entire input is restructured into sequential input of length 16 with a single input having 8 features, denoted by G_i, i = 1 to 16. An input G_i is acted on by the hidden state H_i to produce an output. Certain information is stored in the hidden state H_i and passed to the next step. Therefore, the output

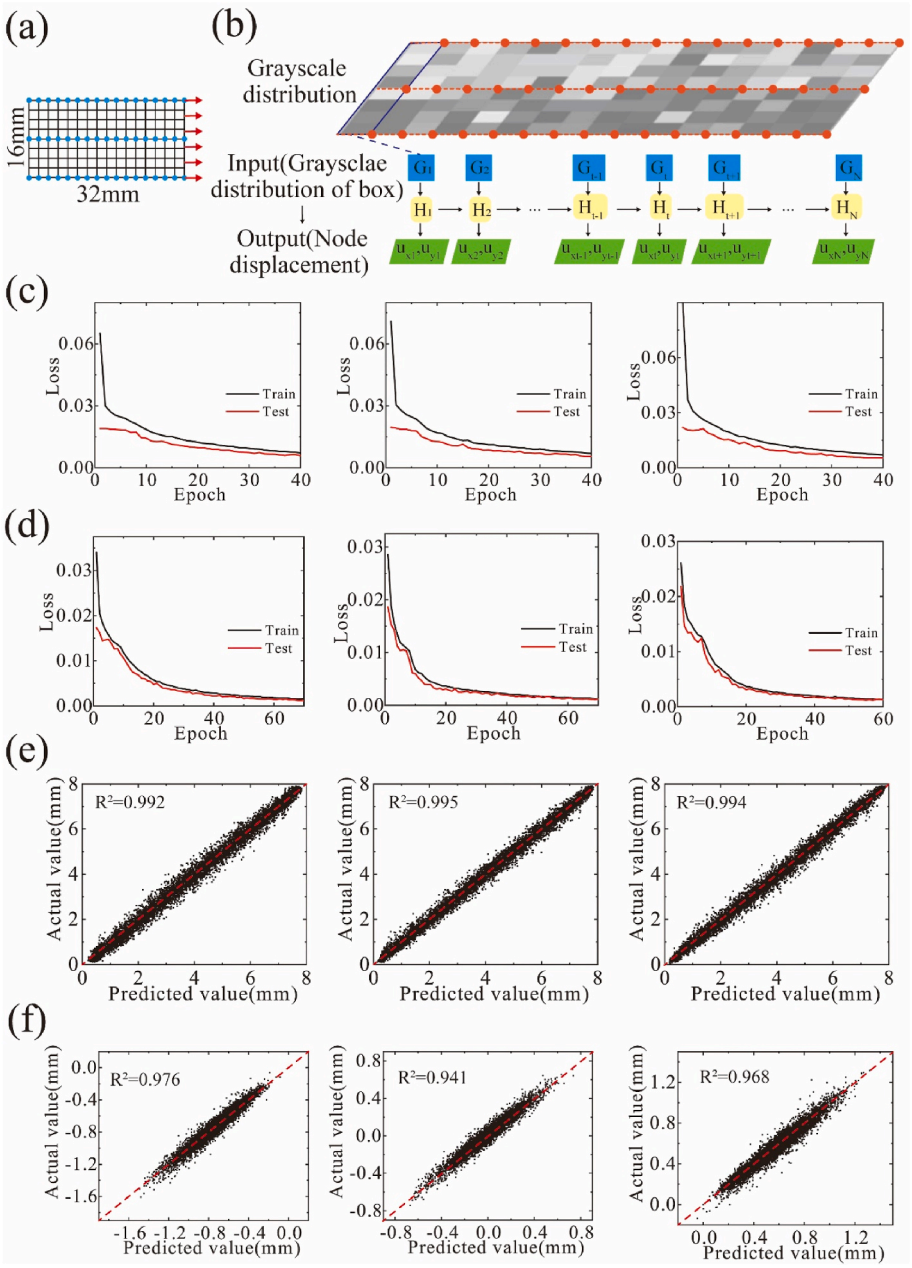

Fig. 2. The RNN-based machine learning model. (a) A rectangular block with 16×8 elements. (b) Inputs, hidden layer and outputs of the RNN model. (c) Training and test loss as a function of epochs showing the training process. (d) Comparisons of actual values and ML predicted values for the nodal displacements.

depends on both the current and previous inputs. The output (size 9) corresponding to each input is the *x*-direction and *y*-direction displacements of the input element u_{xi} and u_{yi}, $i = 1$ to 16.

The adaptive moment estimation optimizer is used to train RNN. Mean squared error (MSE) performs as the loss function to evaluate the accuracy of RNN and is calculated by

$$MSE = \frac{1}{N}\sum_{i=1}^{N}(y_i - \hat{y}_i)^2 \tag{2}$$

where N is the number of the database, y_i is the actual value and $\hat{y}_i$ is the corresponding predicted value. Fig. 2(c) shows the train and test losses versus epochs during the training process of each database, corresponding to the *x*- and *y*-direction displacements of the top, central and bottom nodes. The process is computed using one CPU core (Intel Core i7-10700) and one GPU (NVIDIA GeForce RTX 3060). The loss functions all converge to a steady state. The predicted (ML) and actual (FEM) values of the *x*- and *y*-direction displacements of the top, central and bottom nodes are consistent with high coefficients of determination (R^2 = 0.992, 0.995, 0.994, 0.976, 0.941 and 0.968), indicating the high prediction accuracy of the established ML model (Fig. 2(d)). Note that the ML predictions have much higher efficiency than FEM simulations, reducing the calculation time from hours to seconds.

2.3. Experimental validation

Experiments are conducted to validate the FEM and ML predictions, as shown in Fig. 3. Uniaxial tensile tests were conducted on a universal material testing machine (Instron 68SC-2, USA) at room temperature with a test speed of 5 mm/min. One end of the sample is fixed, while the other end is pulled by a displacement of 8 mm. Four different patterns are used: (a) a longitudinal gradient, (b) a biaxial gradient, (c) a

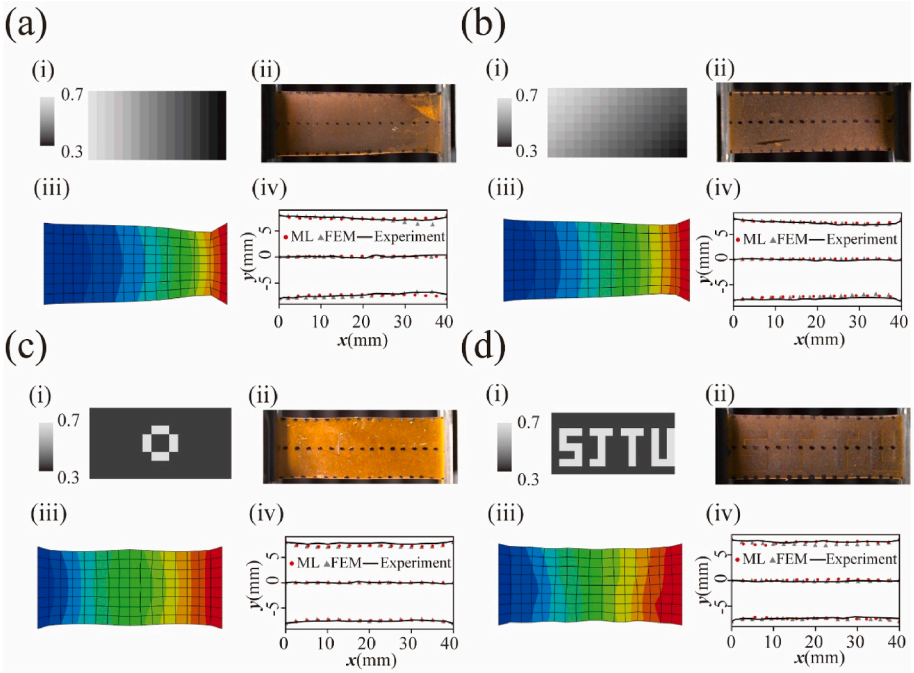

Fig. 3. Comparison of the experimental, FEM simulated and ML predicted deformed shapes with various grayscale distributions. (a)–(d) Four different patterns are shown: (a) a longitudinal gradient, (b) a biaxial gradient, (c) a rectangle pattern, and (d) an "SJTU" pattern. The experimental and FEM simulated deformed shapes are shown in (ii) and (iii). The comparisons between the experimental, FEM simulated and ML predicted deformed curves of the top, central and bottom nodes are shown in (iv).

rectangle pattern, and (d) an "SJTU" pattern.

In the longitudinal gradient pattern (Fig. 3(a)i). G varies linearly from 0.7 on the left side to 0.3 on the right side. The FEM simulated deformed shape at strain = 25% is shown. We then use grayscale DLP 3D printing to fabricate the block using the grayscale longitudinal gradient pattern. Uniaxial tensile tests are conducted for the printed block. The experimental deformed shapes are shown in Fig. 3(a)ii. The top, central and bottom curves of the undeformed structures are marked. The deformed coordinates of the markers are obtained using ImageJ [33]. The experimental, FEM simulated and ML predicted deformed top, central and bottom curves are compared in Fig. 3(a)iv. It can be observed that they all agree well. An obvious necking exists on the right side. Some discrepancies exist, which may result from errors during the 3D printing process and the characterization of the material properties.

Similarly, the ML predicted, FEM simulated, and experimental deformed shapes are compared for the biaxial gradient, rectangle and SJTU patterns in Fig. 3(b)–(d). In Fig. 3(b), the grayscale value varies linearly from the left-top corner ($G = 0.7$) to the right-bottom corner ($G = 0.33$). In Fig. 3(c) and (d), $G = 0.7$ is used to print the central rectangle or the "SJTU" characters, while $G = 0.4$ is used for other regions. It can be seen that all the experimental deformations agree well with the FEM simulations and the ML predictions. Note that the lateral displacements of the rectangular blocks are not obvious, limited by the failure strain of the materials. However, the FEM and ML predictions capture the deformation characteristics in the experiments.

The root mean square errors (RMSE) between the deformed shapes in the ML model and experiments, and in the FEM model and experiments in Fig. 3(a)–(d) are calculated for quantitative comparison. The RMSE of the x and y coordinates of the top, central and bottom curves are shown in Table 1. No apparent dependency between the prediction error and location is observed.

2.4. Machine learning-evolutionary algorithm optimization

ML and EA is integrated to enable the optimization of the deformed shape using grayscale value distribution. ML model performs as a surrogate model with fast calculation. EA is used to search for the optimal grayscale distribution. EA is a biomimetic optimization algorithm inspired by natural selection that simulates the behavior of biological populations. The algorithm begins by creating a random initial population, including 2000 reasonably distributed individuals that satisfy the constraints of the boundary conditions. Each individual is a rectangular block constructed with a random G distribution. The algorithm then iteratively updates the population using the following procedures.

First, each individual is scored by calculating the current fitness value. The fitness function is set as

$$f = \sqrt{\frac{1}{n}\sum_{i=1}^{n}\left(y_1(x_i) - \hat{y}_1(x_i)\right)^2} \tag{3}$$

where n is the number of process goals to be satisfied. x_i is the vector that contains parameters including all the G. $y_1(x_i)$ are the target values and $\hat{y}_1(x_i)$ is the predicted values obtained by the ML model.

Next, the parents and elite subpopulations are selected according to the fitness value. Elite individuals are passed to the next population to form the next generation, while new individuals are generated by parents through crossover and mutation. The iterations stop when the number of generations reaches 12. We choose the number of generations as 12 to reach a balance between accuracy and efficiency. The output results are the optimal G corresponding to the best individual. The ML-EA approach helps to efficiently explore the myriad of possible designs and identify the optimal grayscale distribution, resulting in target deformed shapes.

Two target deformed shapes are used. In Fig. 4(a), the deformed shapes of the top and bottom curves are prescribed as a sine function: $u_y = \sin(\pi x/L)$ mm, where $L = 32$ mm is the original length of the block. The optimized grayscale G distribution is obtained using the ML-EA approach (Fig. 4(a)i). The rectangular blocks are then DLP 3D printed using the optimized grayscale distribution. The experimental and FEM simulated deformed shapes under a 25% strain are shown in Fig. 4(a)ii and iii. The experimental and the ML-EA optimized deformed top and

Table 1
RMSE (mm) between ML and experiments, and FEM and experiments in Fig. 3.

	ML and experiments in (a)	FEM and experiments in (a)	ML and experiments in (b)	FEM and experiments in (b)	ML and experiments in (c)	FEM and experiments in (c)	ML and experiments in (d)	FEM and experiments in (d)
x top	1.58	0.65	0.68	1.24	0.43	0.52	1.15	0.83
y top	0.28	0.34	0.22	0.18	0.46	0.55	0.35	0.46
x central	1.50	0.84	0.78	1.43	0.58	0.48	1.38	0.84
y central	0.17	0.18	0.23	0.21	0.12	0.12	0.3	0.11
x bottom	1.36	0.78	0.59	1.21	0.27	0.28	1.38	0.94
y bottom	0.38	0.29	0.42	0.42	0.16	0.19	0.22	0.27

bottom curves are quantitatively compared with the prescribed sine curved deformation in Fig. 4(a)iv. It can be seen that both the experimental and ML-EA predicted deformed shapes agree well with the prescribed shapes. Note that although the target curves are symmetric, a symmetric material distribution may not be guaranteed by the GA algorithm.

A quadratic displacement along the *x*-direction $u_x = 8 \times (x/L)^2$ mm is prescribed to validate the proposed ML-EA method, as shown in Fig. 4 (b). Similarly, the grayscale distribution is obtained in Fig. 4(b)i. The experimental and FEM simulated deformed shapes are given in Fig. 4(b) ii. The prescribed, experimental and ML-EA predicted displacements of the top, central and bottom curves are shown in Fig. 4(b)iv to Fig. 4(b)vi, respectively. It can be seen the developed ML-EA method can be used to obtain the deformed shapes using optimized grayscale distributions efficiently. Note that there are some discrepancies between the ML-EA predicted and experimental displacements, which could be reduced by increasing the database size.

3. Conclusions

Grayscale DLP 3D printing paves the way to fabricate composites with modulus varying over two orders of magnitude in voxel scale. It has emerged as a novel manufacturing process offering unprecedented design freedom with complex geometries for composites. The minimal size of the material distribution is the same as the pixel size. The material modulus is controlled by varying the grayscale value. Complex composite structures such as functionally graded lattices and composite metamaterials can be easily fabricated and designed.

In summary, we propose an optimization method for grayscale DLP 3D printing structures based on ML and EA in this work. First, the nonlinear mechanical behaviors of the printed materials under various grayscale values are characterized using Mooney-Rivlin constitutive model. Secondly, an automated finite element model-based evaluation is proposed to predict the deformed shapes of the rectangular block and generate the database for the ML model. Deformed shapes with different grayscale distributions are obtained using FEM simulation. Thirdly, an RNN-based ML model is trained using the database to enable fast and precise prediction of the deformed shapes. The ML model accurately predicts deformed top, central and bottom nodal displacements. Finally, optimal designs of the deformed shapes can be efficiently realized by integrating the ML model and EA method. Using the ML-EA approach, sinusoidal and quadratic displacement patterns are designed and validated by experiments. As the relationship between the grayscale value and the output deformation is highly nonlinear, machine learning and evolutionary algorithms can be combined to obtain the objective stress-strain curves fast and efficiently. The ML algorithm is used as a surrogated model which is more efficient than FEM. EA is adopted for fast inverse optimization, which has good global search ability and can quickly search out all solutions in the solution space. The proposed method can be readily used for complex structures, which paves the way for designing and optimizing grayscale digital light processing 3D printed structures.

CRediT authorship contribution statement

Baowen Zhao: Conceptualization, Methodology, Software, Data curation. **Mengjie Zhang:** Validation, Investigation. **Le Dong:** Writing – original draft, preparation. **Dong Wang:** Supervision, Writing – review & editing.

Declaration of competing interest

The authors declare that they have no known competing financial interests or personal relationships that could have appeared to influence the work reported in this paper.

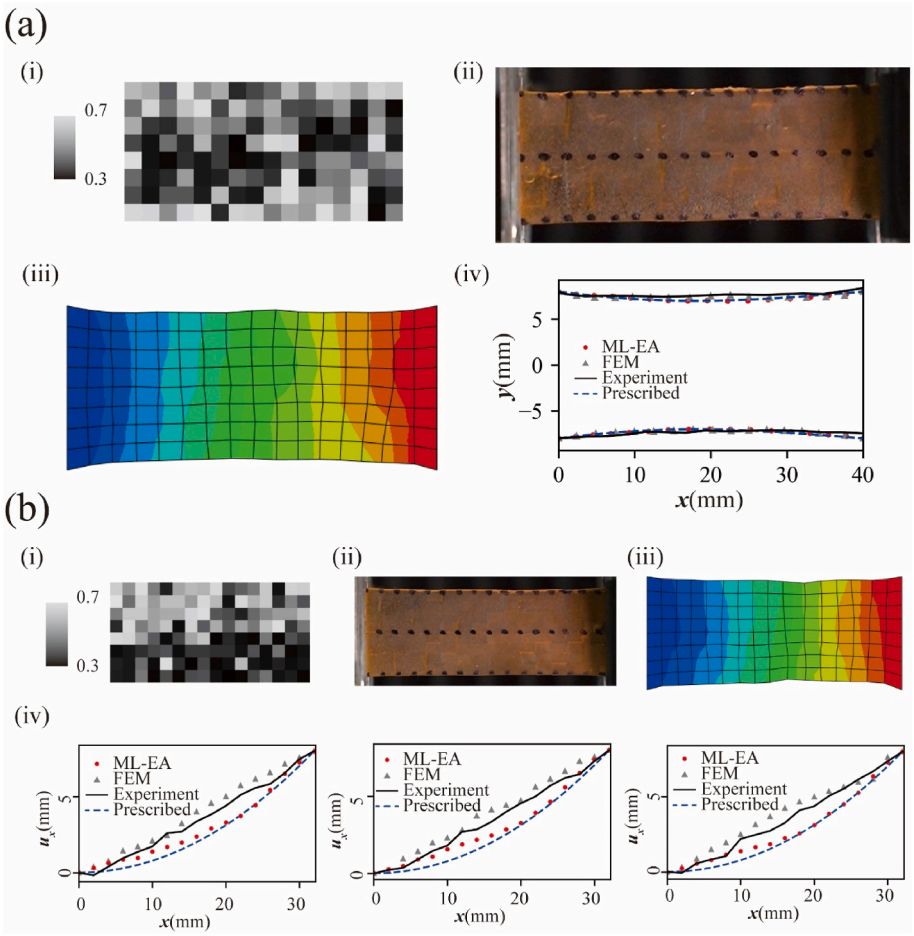

Fig. 4. Optimal design of grayscale gradient using ML-EA method. Two optimal displacements are designed: (a) a sinusoidal displacement along the *y* direction and (b) a quadratic displacement along the *x* direction. The optimized grayscale distribution, experimental and FEM simulated deformed shapes are shown in (i) to (iii). The comparison between the experimental, FEM simulated and ML-EA predicted deformed top, central and bottom curves (iv).

Data availability

Data will be made available on request.

Acknowledgment

D.W. acknowledges support from the National Natural Science Foundation of China (Grant Nos. 52275025, 51905336) and the State Key Laboratory of Mechanical System and Vibration (Grant No. MSVZD202212).

References

[1] H. Yin, Y. Ding, Y. Zhai, W. Tan, X. Yin, Orthogonal programming of heterogeneous micro-mechano-environments and geometries in three-dimensional bio-stereolithography, Nat. Commun. 9 (1) (2018) 4096.
[2] C. Yuan, K. Kowsari, S. Panjwani, Z. Chen, D. Wang, B. Zhang, C.J. Ng, P.V. Y. Alvarado, Q. Ge, Ultrafast three-dimensional printing of optically smooth microlens arrays by oscillation-assisted digital light processing, ACS Appl. Mater. Interfaces 11 (43) (2019) 40662–40668.
[3] Z. Zhao, X. Kuang, C. Yuan, H.J. Qi, D. Fang, Hydrophilic/hydrophobic composite shape-shifting structures, ACS Appl. Mater. Interfaces 10 (23) (2018) 19932–19939.
[4] X. Li, Y. Yang, L. Liu, Y. Chen, M. Chu, H. Sun, W. Shan, Y. Chen, 3D-Printed cactus-inspired spine structures for highly efficient water collection, Adv. Mater. Interfac. 7 (3) (2019).
[5] J. Wang, X. Mu, D. Li, C. Yu, X. Cheng, N. Dai, Modeling and application of planar-to-3D structures via optically programmed frontal photopolymerization, Adv. Eng. Mater. 21 (5) (2019).
[6] I.B. Park, Y.M. Ha, S.H. Lee, Dithering method for improving the surface quality of a microstructure in projection microstereolithography, Int. J. Adv. Manuf. Technol. 52 (5–8) (2010) 545–553.
[7] H. Hingorani, Y.-F. Zhang, B. Zhang, A. Serjouei, Q. Ge, Modified commercial UV curable elastomers for passive 4D printing, Int. J. Soc. Netw. Min. 10 (3) (2019) 225–236.
[8] M.A. Skylar-Scott, J. Mueller, C.W. Visser, J.A. Lewis, Voxelated soft matter via multimaterial multinozzle 3D printing, Nature 575 (7782) (2019) 330–335.
[9] S.G.M. Uzel, R.D. Weeks, M. Eriksson, D. Kokkinis, J.A. Lewis, Multimaterial multinozzle adaptive 3D printing of soft materials, Advanced Materials Technologies 7 (8) (2022).
[10] Z. Ding, C. Yuan, X. Peng, T. Wang, H.J. Qi, M.L. Dunn, Direct 4D printing via active composite materials, Sci. Adv. 3 (4) (2017), e1602890.
[11] C. Yuan, F. Wang, D.W. Rosen, Q. Ge, Voxel design of additively manufactured digital material with customized thermomechanical properties, Mater. Des. 197 (2021).
[12] Z. Xu, R. Hensleigh, N.J.R.K. Gerard, H. Cui, M. Oudich, W. Chen, Y. Jing, X. Zheng, Vat photopolymerization of fly-like, complex micro-architectures with dissolvable supports, Addit. Manuf. 47 (2021).
[13] D. Han, C. Yang, N.X. Fang, H. Lee, Rapid multi-material 3D printing with projection micro-stereolithography using dynamic fluidic control, Addit. Manuf. 27 (2019) 606–615.
[14] K. Kowsari, S. Akbari, D. Wang, N.X. Fang, Q. Ge, High-efficiency high-resolution multimaterial fabrication for digital light processing-based three-dimensional printing, 3D Print. Addit. Manuf. 5 (3) (2018) 185–193.
[15] J. Wu, Z. Zhao, X. Kuang, C.M. Hamel, D. Fang, H.J. Qi, Reversible shape change structures by grayscale pattern 4D printing, Multifunctional Materials 1 (1) (2018).
[16] P. Jiang, C. Yan, Z. Ji, Y. Guo, X. Zhang, X. Jia, X. Wang, F. Zhou, Drawing high-definition and reversible hydrogel paintings with grayscale exposure, ACS Appl. Mater. Interfaces 11 (45) (2019) 42586–42593.
[17] Q. Deng, Y. Yang, H. Gao, Y. Zhou, Y. He, S. Hu, Fabrication of micro-optics elements with arbitrary surface profiles based on one-step maskless grayscale lithography, Micromachines 8 (10) (2017).
[18] M.M. Emami, D.W. Rosen, Modeling of light field effect in deep vat polymerization for grayscale lithography application, Addit. Manuf. 36 (2020).
[19] P. Jiang, Y. Zhang, X. Mu, D. Liu, Y. Liu, R. Guo, Z. Ji, X. Wang, X. Wang, Grayscale stereolithography of gradient hydrogel with site-selective shape deformation, Advanced Materials Technologies 7 (7) (2021).

[20] C. Park, H.J. Bae, J. Yoon, S.W. Song, Y. Jeong, K. Kim, S. Kwon, W. Park, Gradient-wrinkled microparticle with grayscale lithography controlling the cross-linking densities for high security level anti-counterfeiting strategies, ACS Omega 6 (3) (2021) 2121–2126.
[21] E. Guven, Y. Karpat, M. Cakmakci, Improving the dimensional accuracy of micro parts 3D printed with projection-based continuous vat photopolymerization using a model-based grayscale optimization method, Addit. Manuf. 57 (2022).
[22] J.E. Hergert, A.C. Uzcategui, A. Muralidharan, V. Crespo-Cuevas, V.L. Ferguson, R. R. McLeod, Grayscale digital light processing and post-treatment for the fabrication of 3D-printed polymer blends, Adv. Eng. Mater. 24 (8) (2022).
[23] G.I. Peterson, J.J. Schwartz, D. Zhang, B.M. Weiss, M.A. Ganter, D.W. Storti, A. J. Boydston, Production of materials with spatially-controlled cross-link density via vat photopolymerization, ACS Appl. Mater. Interfaces 8 (42) (2016) 29037–29043.
[24] Z. Zhao, J. Wu, X. Mu, H. Chen, H.J. Qi, D. Fang, Origami by frontal photopolymerization, Sci. Adv. 3 (4) (2017), e1602326.
[25] A. Muralidharan, A.C. Uzcategui, R.R. McLeod, S.J. Bryant, Stereolithographic 3D printing for deterministic control over integration in dual-material composites, Adv Mater Technol 4 (11) (2019).
[26] M.J. Mirzaali, A. Herranz de la Nava, D. Gunashekar, M. Nouri-Goushki, R.P. E. Veeger, Q. Grossman, L. Angeloni, M.K. Ghatkesar, L.E. Fratila-Apachitei, D. Ruffoni, E.L. Doubrovski, A.A. Zadpoor, Mechanics of bioinspired functionally graded soft-hard composites made by multi-material 3D printing, Compos. Struct. 237 (2020).
[27] S.M. Montgomery, H. Hilborn, C.M. Hamel, X. Kuang, K.N. Long, H.J. Qi, The 3D printing and modeling of functionally graded Kelvin foams for controlling crushing performance, Extrem. Mech. Lett. 46 (2021), 101323.
[28] S.M. Montgomery, C.M. Hamel, J. Skovran, H.J. Qi, A reaction–diffusion model for grayscale digital light processing 3D printing, Extrem. Mech. Lett. 53 (2022).
[29] X. Peng, L. Yue, S. Liang, S. Montgomery, C. Lu, C.M. Cheng, R. Beyah, R.R. Zhao, H.J. Qi, Multi-color 3D printing via single-vat grayscale digital light processing, Adv. Funct. Mater. 32 (28) (2022).
[30] X. Kuang, J. Wu, K. Chen, Z. Zhao, Z. Ding, F. Hu, D. Fang, H.J. Qi, Grayscale digital light processing 3D printing for highly functionally graded materials, Sci. Adv. 5 (5) (2019), eaav5790.
[31] J. Wang, N. Dai, C. Jiang, X. Mu, B. Zhang, Q. Ge, D. Wang, Programmable shape-shifting 3D structures via frontal photopolymerization, Mater. Des. 198 (2021).
[32] I. Valizadeh, O. Weeger, Parametric visco-hyperelastic constitutive modeling of functionally graded 3D printed polymers, Int. J. Mech. Sci. 226 (2022).
[33] C.A. Schneider, W.S. Rasband, K.W. Eliceiri, NIH Image to ImageJ: 25 years of image analysis, Nat. Methods 9 (7) (2012) 671–675.